



Production and Characterization of Oxides Formed on Grade 300 and 350 Maraging Steels Using two Oxygen/Steam Rich Atmospheres

Mauro Andrés Cerra Florez^{a,b,c,*}, Gemma Fargas Ribas^{b,c}, Joan Josep Roa Rovira^{b,c},
Antonio Manuel Mateo García^{b,c}, Marcos Natan da Silva Lima^{a,c}, Guiomar Riu Perdrix^{b,c} ,
Jorge Luiz Cardoso^a , Marcelo José Gomes da Silva^a

^aUniversidade Federal do Ceará, Departamento de Engenharia Metalúrgica e de Materiais, Campus do Pici, bloco 729, 60440-554, Fortaleza, CE, Brasil.

^bUniversitat Politècnica de Catalunya, Escola d'Enginyeria de Barcelona Est, Departamento de Ciencia e Ingeniería de Materiales, Eduard Maristany 10-14, 08019, Barcelona, España.

^cUniversitat Politècnica de Catalunya, Escola d'Enginyeria de Barcelona Est, Centro de Investigación de Barcelona en Ciencia e Ingeniería Multiescala, Eduard Maristany 10-14, 08019, Barcelona, España.

Received: June 13, 2022; Revised: August 16, 2022; Accepted: October 06, 2022

The growing process of a spinel-like oxide film can be obtained through different atmospheres; in this sense Air, O₂, steam, and nitrogen atmospheres were used in different steps during the aging heat treatment at 490°C of maraging 300 and 350 alloys. The oxidation layer produced under different atmospheres was chemically, microstructurally and mechanically characterized by means of advanced techniques. The results showed (in both alloys) a non-homogeneous mix oxide formed by magnetite, nickel and cobalt ferrites and MoO₃ heterogeneously distributed along the oxide thickness. It was also founded TiO₂ in the innermost areas and a particularly important quantify of hematite on the external surface. A nickel-rich austenite phase was produced at the interphase due to the combination of nickel stability and the preference of cobalt, molybdenum, and iron diffuses through the film as ions. The highest thickness values were found in the oxides produced in maraging 300 steels which could indicate greater susceptibility to oxidation comparing with grade 350 maraging steel. The oxide films produced in both maraging alloys using air atmosphere presents excellent adherence, and the results show the capability for being used for tribological applications under sliding contact tests.

Keywords: *maraging alloys, oxidation treatment, oxide film, XRD analysis, raman analysis, nanoscratch study.*

1. Introduction

Maraging alloys present a microstructure with ductile martensite (α') rich in nickel and with intermetallic compounds precipitated during the aging treatments - like Ni₃(Ti,Mo) and Fe₂(Ti,Mo), increasing strongly their mechanical resistance under service condition¹⁻⁹. Their excellent mechanical properties make these materials useful to be used in different industrial sectors such as the aeronautic, military, among others^{1,2}. Furthermore, these alloys are widely employed in several components of some ultracentrifuges used in the nuclear industry to enrich uranium. In these applications, maraging alloys are exposed in corrosive atmospheres due to the presence of fluorine and eventually fluoride acid impurities⁹.

The only scientific article that confirms the use of a previous oxidation process in maraging steels used in the nuclear industry is from Glaser et al.¹⁰, they related a pre-oxidation process for enhance the corrosion resistance by creating a duplex oxide layer microstructure of spinel and hematite. In the literature, several authors studied the

oxidation process of some maraging steels under separated atmospheres (CO₂, steam, oxygen and air), but the most important details of the procedures used were not described.

Regarding the gas centrifuges for the nuclear industry, an important application demanding high mechanical resistance alloys, high-strength aluminum alloys were early used for the rotors, but nowadays these rotors are made from higher tensile strength materials as maraging steels, resulting in speed increase of these rotors.¹¹ Another problem cited in literature when using maraging steel in environment containing oxides is the crack susceptibility, mainly in reactions that produce hydrogen.¹²

Klein et al.¹³⁻¹⁵ in the 80's studied the oxidation of Fe-18Ni-8.5Co, Fe-29Ni-17Co and the 250 maraging steels using air, CO₂, oxygen and superheated steam (in separated processes) during the aging heat treatment at 485 °C for 3 h. In the oxide films formed in all the steels for the investigated atmospheres, a mix of hematite and only the iron spinel (Fe₃O₄) were found.

In the 90's, Rezek et al.¹⁶ investigated the superheated steam flow effect during the aging of 250 maraging steel grade.

*e-mail: mauro.cerra@ufc.br

Through this research, it was found that depending on the flow, differences on the oxide layer thicknesses are induced. Using a low flow - 0.2 m³/h, thin layers formed by a mix of hematite and magnetite are produced, whereas for thick oxide layer (formed by using high gas flow - 6 m³/h) mainly is constituted by magnetite phase. Greyling et al.¹⁷ studied the oxidation formation process on 300 maraging steel during the heat treatments in air atmosphere using different temperatures. They found that oxidation kinetics occurs by the transport of reactant gas and metal species through the oxide layer.

Recently, Florez et al.¹⁸ used a similar procedure for produce a spinel-like oxide film, in this case, CO₂ in the first step was used. They found an oxide formed by hematite and mainly the cobalt spinel (CoFe₂O₄).

Within this context, in the present article, an oxide layer was produced on 300 and 350 maraging alloys by using a novel procedure with the combination of atmospheres (synthetic air, water steam, N₂ and O₂, water steam, N₂) at 490 °C, procedure adapted to the applied by Florez et al.¹⁸. Subsequently, the spinel layer for both maraging alloys was chemically, microstructurally and also tribologically investigated at the micrometric length scale.

2. Materials and Methods

2.1. Material

Two different sets of maraging alloys were investigated, 300 and 350, and their chemical composition is summarized in Table 1.

Initially, samples (1,0 cm x 1,0 cm x 2,0 cm) were annealed at 840 °C for 1 h. Prior to the growing process under different atmospheres, the maraging alloys were

ground/polished using SiC paper up to 6 mm. After that, the specimens were ultrasonically cleaned by using ethanol for 15 min and subsequently dried using pure air.

The aging heat treatment was performed in a tube oven with a gas inlet connected to 4 lines, one connected to a steam generator and the other three connected to O₂, synthetic air and N₂ cylinders. The steam generator was tempered at 150 °C and it was connected to helium injection as a carrier gas to increase the flow rate. A scheme of the set-up used is presented in Figure 1.

The two maraging 300 and 350 alloys were heated at 300 °C for 30 min under different atmospheres. Steam was added and the temperature was increased to 490 °C for 15 min. Shortly thereafter, the O₂ or synthetic air gas was removed, and the temperature was kept constant at 490 °C for 3 h only with steam and helium (600 mL/min). The cooling step until room temperature was performed for 3 h with a N₂ flow to avoid over oxidation of the maraging alloys.

2.2. Chemical and microstructural characterization

The oxide layer morphology was investigated by using laser scanning confocal microscopy (LSCM) Carl ZEISS LSM 800 and white light interferometry (WLI) Veeco Wyko 9300NT. Using these techniques, several roughness parameters, including the arithmetic mean height (Sa), the maximum height (Sz), the maximum peak height (Sp), the maximum pit height (Sv) and the root mean square height (Sq) were obtained. More information about the meaning of each parameter is available in¹⁹⁻²¹. The software used to treat the different images and obtain the main morphological parameters presented above was the Profilonline Filmetrics® software. The Phenom XL Desktop scanning electron microscopy (SEM)

Table 1. Chemical composition of both maraging alloys (% wt.).

	Ni	Co	Mo	Ti	Cr	V	Si	Al	C	Fe
Mar 300	18.28	9.51	4.80	0.73	0.12	0.10	0.08	0.07	< 0.01	Bal.
Mar 350	17.65	11.65	4.69	1.44	0.05	0.10	0.04	0.06	0.002	Bal.

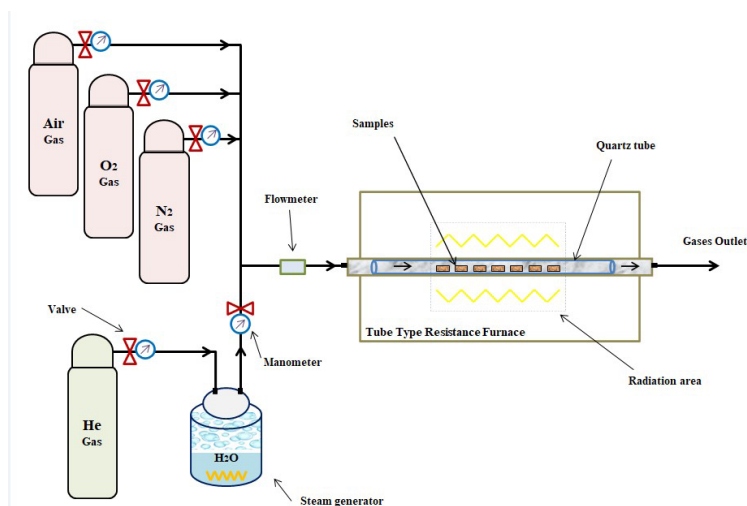


Figure 1. Experimental configuration of the devices for the aging heat treatment.

coupled with energy-dispersive spectroscopy (EDS) detector to observe the oxide and obtain the chemical composition of the different oxide layers were used. The thickness of the oxide layer for each investigated system was analyzed by focused ion beam (FIB) milling of cross-sections and field emission scanning electron microscopy (FE-SEM) inspection. A dual-beam workstation, Zeiss Neon 40 (Carl Zeiss) was also used. Ga^+ ion source was used to mill the surface at a voltage of 30 kV. The final polishing process of the cross-section was performed at a current of 500 pA and 30 kV acceleration voltage.

For the detection of the phases present in the steels, X-ray diffraction (XRD) analysis was performed on the Philips X'Pert equipment using a $\text{CoK}\alpha$ radiation source with a wavelength of 1.789 nm and monochromator. The 2θ varied from 10 to 110° , the angular step was 0.02° with 3 s per scan. Voltage and current were held constant and equal to 40 kV and 45 mA, respectively. The analysis of the patterns found was carried out in the X'PertHighScore Plus® (Panalytical®) software and the % of each constitutive phase present in the oxide layer were quantified using the reference intensity ratio (RIR) based in the literature^{22,23} for the same software.

Raman spectroscopy (Renishaw's inVia Qontor) was used to identify the different components present in the oxide layer. The measurements were carried out with a neon laser with a wavelength of around 532 nm. The data were treated using Wire™ software.

2.3. Sliding properties

Nano-scratch tests were carried out with a Nanoindenter XP (MTS). A Berkovich indenter tip was used to scratch the surface of interest. The different tests were done under load control mode – the load was increased linearly - at a velocity of 10 mm/s for a total scratch length of 500 mm up to a maximum load of 100 mN. Three different scratches were performed on each sample. The distance between scratch was held constant and equals to 500 μm to avoid any overlapping effect. The scratches marks were observed by using the Phenom XL Desktop SEM microscope. The test procedure was used following the recommendations indicated by Florez et al.¹⁸.

3. Results and Discussion

The results of XRD for the maraging 300 and 350 alloys before inducing the oxide layer (also labeled as reference samples) can be seen in Figure 2. Three main peaks are visible in both spectra: $\{110\}$, $\{200\}$ and $\{211\}$, which corresponds to martensite α' in agreement with the data reported in^{24,25}.

Figure 3 shows the XRD spectra of the different oxide layers growth in both maraging alloys investigated. Two different heat treatments were analyzed; (1) oxide layer produced in Air/Steam/ N_2 atmospheres (Figure 3a) and (2) produced in O_2 /Steam/ N_2 atmospheres (Figure 3b). All oxide layers presented the same kind of phases labeled as A, B, C, D and E. The phase labelled as A, which corresponds to a spinel ferrite, present the following peaks $\{111\}$, $\{112\}$, $\{121\}$, $\{004\}$, $\{321\}$ and $\{224\}$ in the XRD spectrum in agreement with^{18,26,27}. The peaks identified for the phase B in the XRD spectrum are: $\{012\}$, $\{104\}$, $\{110\}$, $\{113\}$, $\{024\}$, $\{116\}$ and $\{214\}$ correspond to hematite (Fe_2O_3) according

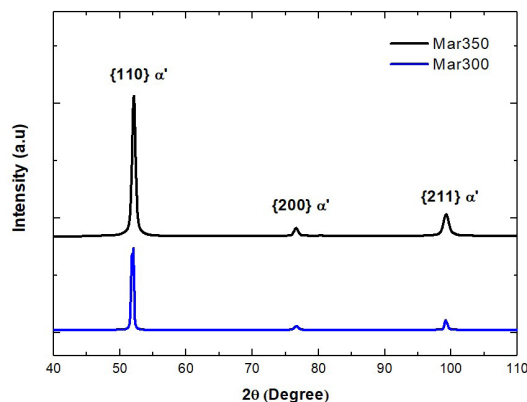


Figure 2. X-ray diffraction (XRD) spectra for the different reference maraging alloys investigated here.

to JCPDS No.084-0308²⁶. In C, the peaks $\{110\}$, $\{101\}$ and $\{200\}$ were identified as the titanium oxide (TiO_2) according to JCPDS No.034-0180²⁶. Furthermore, the XRD spectrum show several peaks $\{002\}$, $\{-112\}$, $\{022\}$, $\{220\}$ and $\{112\}$ labelled as D phase and identified as molybdenum oxide (MoO_3) according to JCPDS No.080-0347²⁶ and also as reported by Zhao et al.²⁸. In E, it is possible to see two different peaks - $\{111\}$ and $\{200\}$ - that correspond to the austenitic (γ -) phase^{18,25}, which is rich in Ni, Fe and Co in agreement in^{13-16,18}. The γ -phase is formed during the oxidation process, when iron (Fe), cobalt (Co), molybdenum (Mo) and titanium (Ti) diffuses through the layer, leaving the maraging alloy surface with a high nickel content.

The phase composition obtained by XRD spectra and present in the different oxide layers produced on maraging 300 and 350 alloys under different atmospheres are summarized in Table 2.

The values of the phase's quantification performed on the oxides showed similar amount of each compound for all conditions. The oxides produced on the maraging 350 alloy under different investigated conditions presented the lowest proportion of spinel, however, a greater amount of MoO_3 and TiO_2 is evident. This phenomenon may be related to the greater amount of Co and Ti in the chemical composition of the maraging 350 alloy (see Table 1). This effect is in agreement with the data reported in^{1,7,18,29,30}, and it is attributed that the thermal treatment helps to increase the number of intermetallic precipitates rich in Mo and Ti along with the oxide layer. The amount of hematite formed in all oxides is relatively similar, which indicates that, although two different atmospheres were used in the first stages, in both processes the kinetic and thermodynamic conditions are favorable to produce the formation of this phase.

Figures 4 and 5 exhibit the optical (left-hand side) and laser scanning confocal microscope (LSCM) (right-hand side) micrographs of the oxide layer for the air/steam/ N_2 and O_2 /steam/ N_2 atmosphere for each investigated system, respectively. As it is evident, all the different layers present the same type of heterogeneities, such as ridges, valleys, cracks and peeling. These defects were created due to the difference in volume, thermal expansion coefficient and density between the different constitutive phases that form

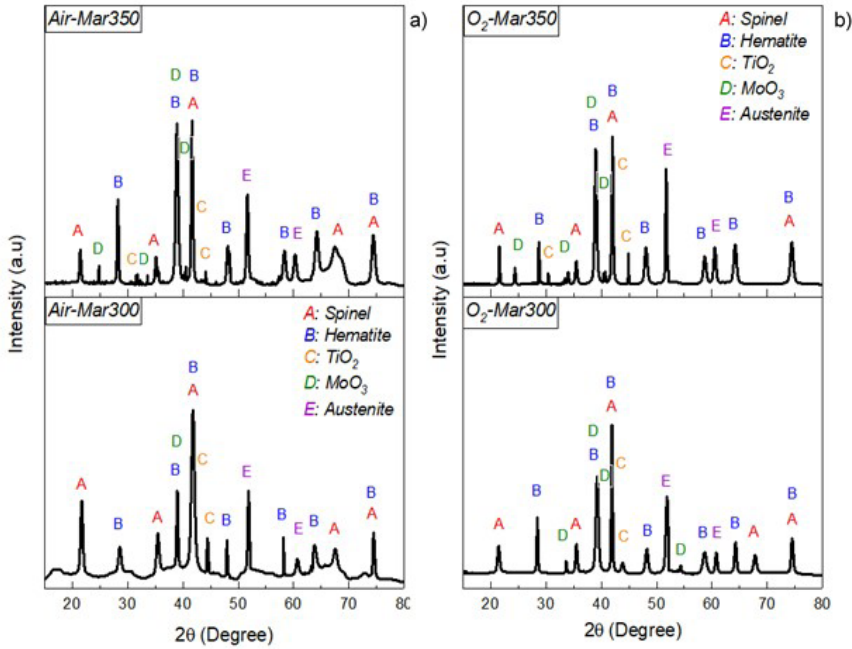


Figure 3. X-ray diffraction spectra of the different oxides produced under different atmospheres for each maraging alloy.

Table 2. Vol. % content for each constitutive phase present in the oxide layer produced in both maraging alloys.

Atmosphere	Steel	Vol. % Spinel	Vol. % Hematite	Vol. % MoO ₃	Vol. % TiO ₂
Air/Steam/N ₂	M300	45	47	5	3
	M350	44	42	9	5
O ₂ /Steam/N ₂	M300	43	51	5	1
	M350	42	45	9	4

Table 3. Roughness parameters (in μm) for each investigated system according to ISO 25178.

Roughness parameter	Air/Steam/N ₂ - Mar300	Air/Steam/N ₂ - Mar350	O ₂ /Steam/N ₂ - Mar300	O ₂ /Steam/N ₂ - Mar350
Arithmetic mean height (S_a)	0.18	0.18	0.22	0.17
Maximum Height (S_z)	2.41	2.09	3.21	2.29
Maximum Peak Height (S_p)	0.85	0.83	1.66	1.10
Maximum Pit Height (S_v)	1.56	1.26	1.55	1.19
Root Mean Square Height (S_q)	0.22	0.23	0.28	0.22

the oxide layer, as well as external factors such as vapor condensation on the surface, which can help the creation of these defects.

Figure 6 shows the 3D topography image ($650 \times 470 \mu\text{m}^2$) obtained by interferometry of each investigated specimen. In the images, it is possible to see a heterogeneous surface with several nodules, high peaks and deep valleys along the surface that suggests a non-uniform growing process.

The main roughness parameters (S_a and S_z) are described in Table 3. As it is evident in these images, the bands that appear in the interferometric images are related to the ground/polishing patterns induced prior to the oxidation process.

Furthermore, the S_a is similar for all the different investigated samples, although the surface of the oxide produced in the maraging 300 alloy under Air/Steam/N₂ atmospheres presents greater variations between the highest peak and the deepest valley. The small differences found between the roughness of the samples do not indicate any relationship with the chemical composition of the steels and perhaps they are more reactive with the heat treatment itself.

Figure 7 shows SEM micrographs of the oxide layer produced under Air/Steam/N₂ atmosphere on maraging 300 alloy. In Figure 7a the oxide layer looks like homogeneous, with high content of defects, like porosity, nodules (Figures 7b and 7c).

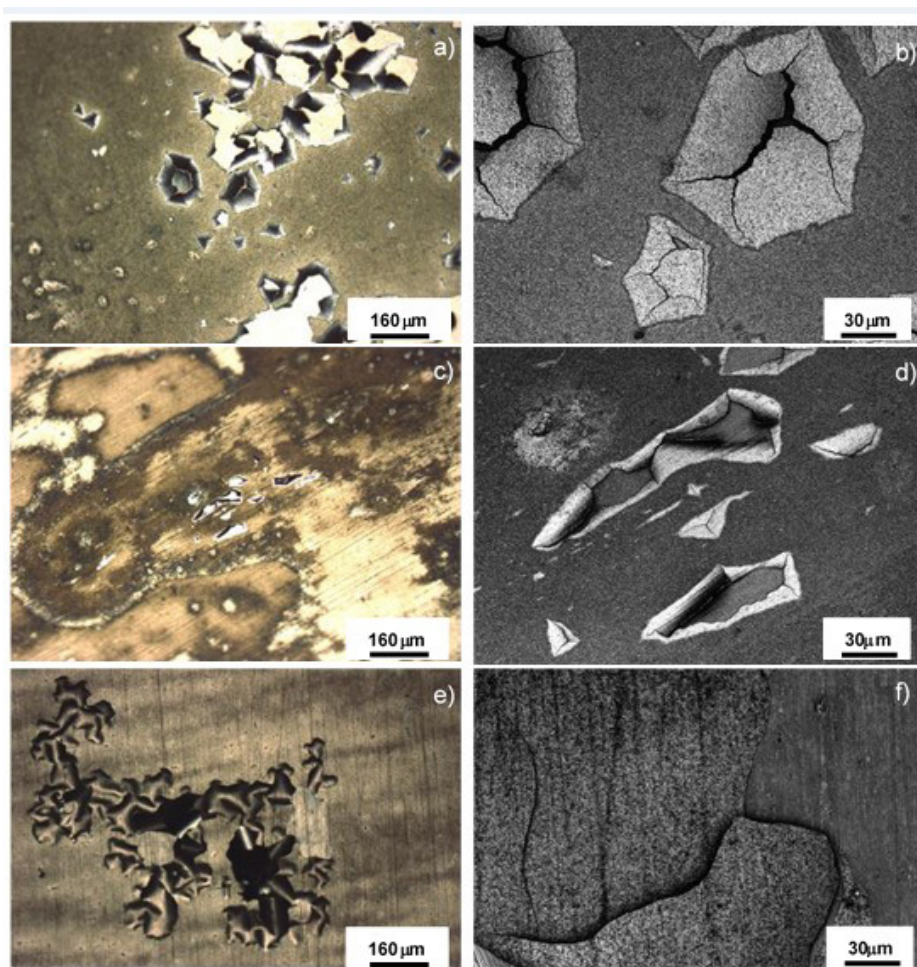


Figure 4. Optical (a, c, e) and laser scanning confocal microscope - LSCM (b, d, f) micrographs of several defects heterogeneously distributed on the oxide layer produced under air/steam/ N_2 atmosphere for each maraging alloy.

Table 4. Summary of the chemical composition determined by EDS measurements taken at different positions (see Figure 7c).

EDS quantitative analysis from points A, B and C (wt.%)				
Elem. Number	Elem. Symbol	Point A	Point B	Point C
26	Fe	57.5	58.5	63.5
8	O	34.0	34.9	29.7
27	Co	4.8	6.2	4.3
28	Ni	2.9	0.5	2.00
42	Mo	0.7	0.3	0.5
22	Ti	0.1	0.1	-

Table 4 summarizes the chemical composition obtained by energy-dispersive X-ray spectroscopy (EDS) near the nodule as depicted in Figure 7c.

These measurements show that there are variations in its chemical composition, therefore, the typical area of the oxide (with greater porosity) presents a high Co content (point B in Figure 7c), while in the upper region of the nodule (point A in Figure 7c) presents a high Ni and Mo content. Also, it is necessary to highlight that in the different regions the Fe content is homogeneous, while the content of Ti changes considerably. At points A

and B, the Ti content is homogeneous while at point C is deficient of this element. It is essential to indicate that in this research, the EDS oxygen value was only taken into account for comparative purposes.

Figure 8 exhibits the SEM micrographs of the different heterogeneities dispersed in the oxide layer for the maraging 350 alloy growth under Air/Steam/ N_2 atmosphere, such as protuberances, cracks, ridges and oxide decohesion.

Four different chemical measurements were done by energy-dispersive X-ray spectroscopy (EDS) (see Figure 8c) and summarized in Table 5.

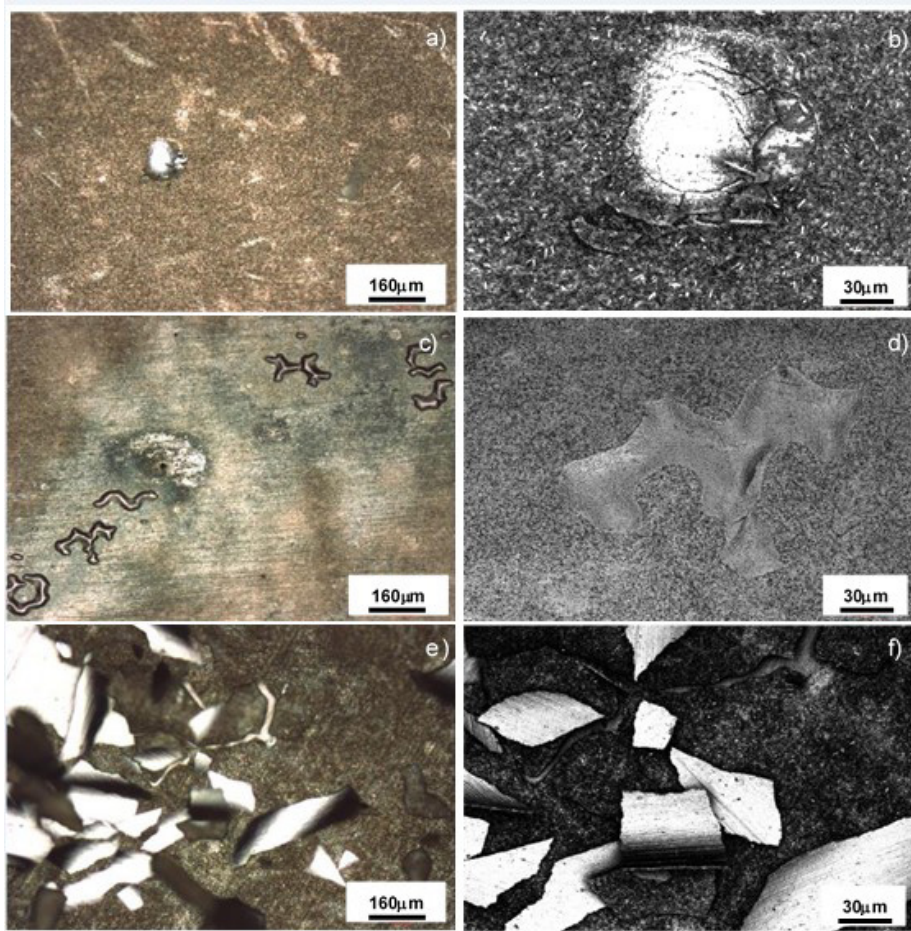


Figure 5. Optical (a, c, e) and laser scanning confocal microscope - LSCM (b, d, f) micrographs of several defects heterogeneously distributed on the oxide layer produced under O_2 /steam/ N_2 atmosphere for each maraging alloy.

Table 5. Summary of the chemical composition determined by EDS measurements taken at different position indicated in Figure 8c.

EDS quantitative analysis from points A, B, C and D (wt. %)						
Elem. Number	Elem. Symbol	Point A	Point B	Point C	Point D	
26	Fe	38.8	48.5	53.4	67.0	
8	O	19.9	22.0	30.3	29.4	
27	Co	11.3	7.2	4.8	2.3	
28	Ni	17.6	9.5	4.1	0.5	
42	Mo	10.3	10.5	6.2	0.7	
22	Ti	2.1	2.3	1.2	0.1	

On the other hand, Figure 9 shows the SEM micrographs for the oxide layer growth under O_2 /Steam/ N_2 atmosphere on maraging 300 alloy. These micrographs show similar kinds of defects (such as cracks and ridges). The chemical composition near an oxide defect is summarized in Table 6.

The quantification on the Tables 5 and 6 confirms the existence of an element concentration profile in the different oxide layer, the inner base is richer in elements such as nickel, titanium, cobalt and molybdenum, and in the upper part the iron is abundant.

The surface of the oxide layer produced under O_2 /Steam/ N_2 atmospheres on maraging 350 alloy is shown in Figure 10,

where some heterogeneities like protuberances are clearly visible (see Figure 10a and 10b). SEM magnification of this defect is appreciated in Figure 10c. Also, in this image, two different punctual EDS analysis was also carried out on and also at the vicinity of the defect to determine the chemical composition (see Table 7).

The chemical composition and morphological differences indicate the existence of different phases or compounds dispersed in the surface of the oxide in fair agreement with the XRD spectra presented in Figure 3.

SEM micrographs in Figure 11a, 11c, 11e, 11g shows a line scan (white dash line), EDS analysis (Figure 11b, 11d, 11f, 11h)

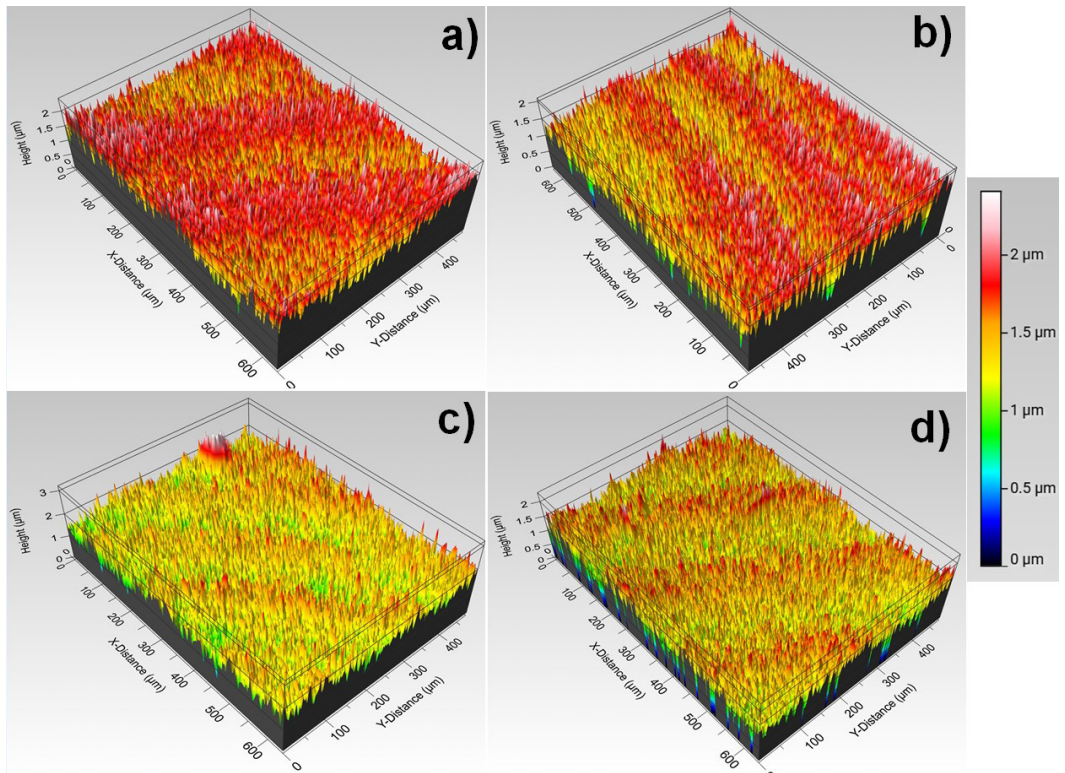


Figure 6. Interferometry 3D topography of the oxide surface produced in O₂ atmosphere (a) maraging 300 alloy and (b) maraging 350 alloy, and in Air atmosphere (c,d) maraging 300 alloy and maraging 350 alloy respectively.

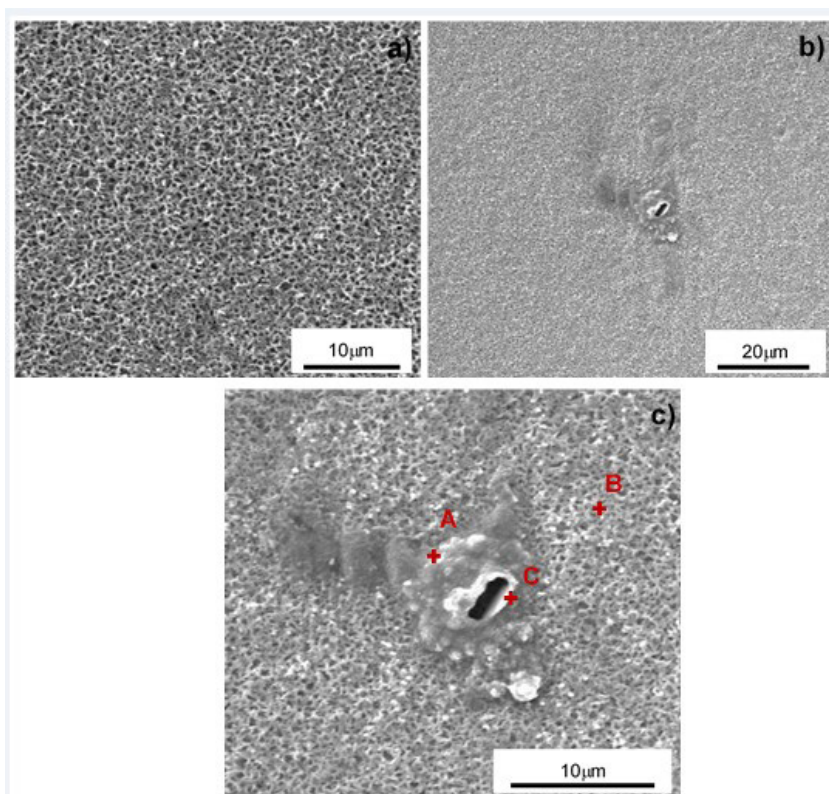


Figure 7. SEM micrographs of the oxide layer on maraging 300 alloy growth under Air/steam/N₂ atmospheres.

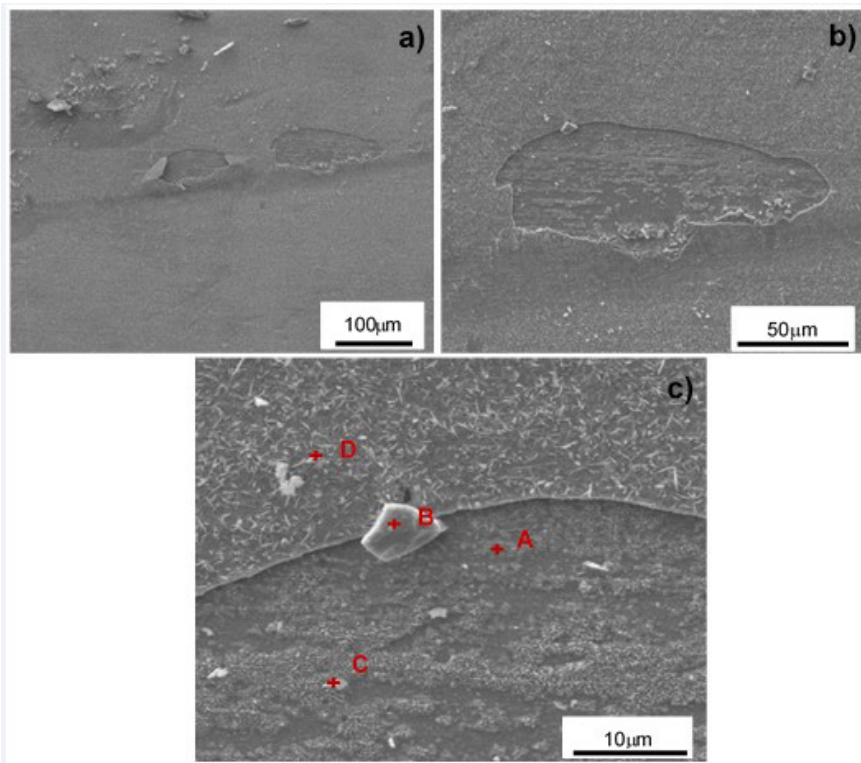


Figure 8. SEM micrographs of the oxide layer growth under air/steam/N₂ on maraging 350 alloy.

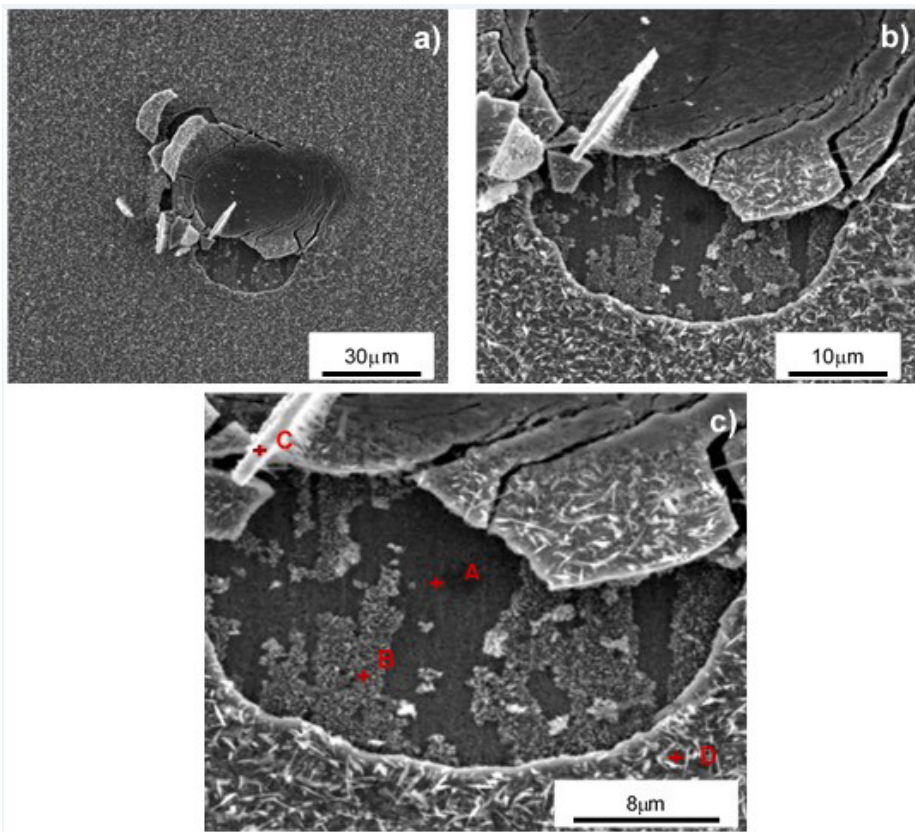
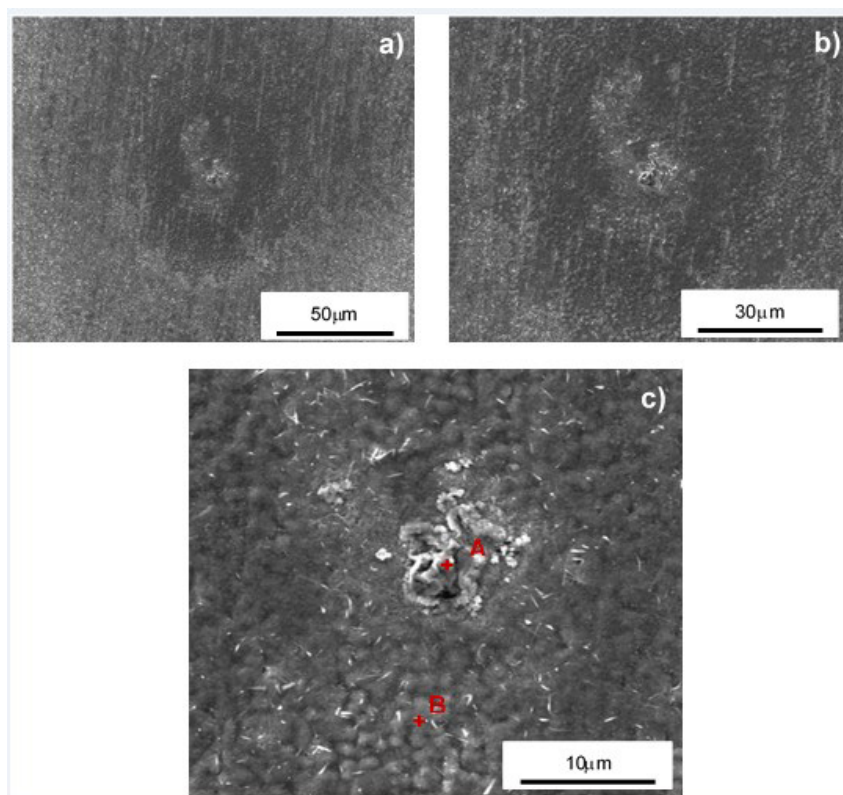


Figure 9. SEM micrographs of the oxide layer growth under O₂/steam/N₂ atmosphere on maraging 300 alloy.

Table 6. Summary of the chemical composition determined by EDS measurements taken at the different positions indicated in Figure 9c.

EDS quantitative analysis from points A, B, C and D (wt. %)						
Elem. Number	Elem. Symbol	Point A	Point B	Point C	Point D	
26	Fe	46.2	55.0	63.7	66.9	
8	O	20.7	34.0	36.3	28.9	
27	Co	8.3	4.1	-	2.7	
28	Ni	13.3	2.4	-	0.7	
42	Mo	10.4	4.1	-	0.7	
22	Ti	1.1	0.4	-	0.1	

**Figure 10.** SEM micrographs of the oxide layer growth under O_2 /steam/ N_2 atmosphere on maraging 350 alloy.

crossing the main defects present in the oxide layer of each maraging alloys investigated here.

In the chemical profiles through the defect present on the oxide layer by using air/steam/ N_2 atmospheres on maraging 300 alloys, it is possible to see a rectangular shape with straight edges. This inclusion is rich in Ti that corresponds to a specific defect of the material. It is well investigated that in these alloys with an appreciable Ti and N content, it is possible the formation of titanium nitrides (TiN) during the solidification process^{18,31,32}. On the other hand, for the oxide layer present in maraging 350 alloys under air/steam/ N_2 atmospheres, the chemical composition map shows the composition differences between the inner layer (rich in Ni, Mo, Co and Ti) and the outer layer is rich in Fe. This differential in composition is in agreement with the finding reported in^{13-15,18}. Figure 11e-h show the surface oxide layer growth under O_2 /steam/ N_2 atmospheres on maraging 300 and 350 alloys, respectively. Two types of holes are clearly visible. The hole seen on maraging

300 alloy presents an increase of Ni, Co, Ti and Mo content. This phenomenon can be attributed to an enrichment area of intermetallic compounds like Ni_3Ti , Ni_3Mo , Fe_3Ti , and Fe_3Mo that precipitate during the aging treatment of maraging steels in concordance with^{1,4,18,33-35}. It is worthily to mention that these intermetallic phases are very stable and do not form oxides, breaking the homogeneity of the oxidized layer. On the other hand, the oxide layer growth on maraging 350 alloy shows a hole with an increase in the Mo and Ti content. This can be associated with two different phenomena: the presence of TiN and the presence of the different intermetallic compounds (Ni_3Ti , Ni_3Mo , Fe_3Ti , and Fe_3Mo) that do not form oxides. Comparing the microstructural defects present in the oxide layer as well as the chemical composition determined by EDS, both maraging alloys present the same typology of defects and the chemical composition are more or less similar.

For the identification spinels types formed on the samples, Raman spectroscopy technique was used. Figure 12a and 12b

show the Raman spectrum obtained from the oxide layer growth under Air/Steam/N₂ and O₂/Steam/N₂ atmospheres on both alloys, respectively.

Table 7. Summary of the chemical composition determined by EDS measurements taken at the different positions indicated in Figure 10c.

EDS quantitative analysis from points A and B (wt. %)			
Elem. Number	Elem. Symbol	Point A	Point B
26	Fe	41.7	56.1
8	O	38.0	34.0
27	Co	5.5	5.3
28	Ni	3.0	2.2
42	Mo	11.5	2.0
22	Ti	0.3	0.4

It is possible to find the same species in all the spectrums. Three spinels were found, iron ferrite (Fe₃O₄) labeled as A, with the bands located at 302, 460, 616, 660 and 690 cm⁻¹ in agreement with^{36,37}, nickel ferrite (NiFe₂O₄) identified as B, with the bands at 195, 316, 470 and 679 cm⁻¹ according to^{38,39} and cobalt ferrite (CoFe₂O₄) labeled as C and located in the bands 300, 465, 615, and 679 cm⁻¹ also found in^{18,38-41}. Hematite (Fe₂O₃) with the bands located at 227, 246, 293, 412, 500, 611 and 1321 cm⁻¹ was also found^{18,42,43} labeled as D, and the molybdenum oxide (MoO₃) was also identified (E) by the bands at 280, 663, 816 and 901 cm⁻¹ according to⁴⁴⁻⁴⁷. With this result, the existence of all expected spinels was confirmed.

The examination and the determination of the oxide layer thickness are essential to reach a proper understanding of the oxidation process under the different atmospheres

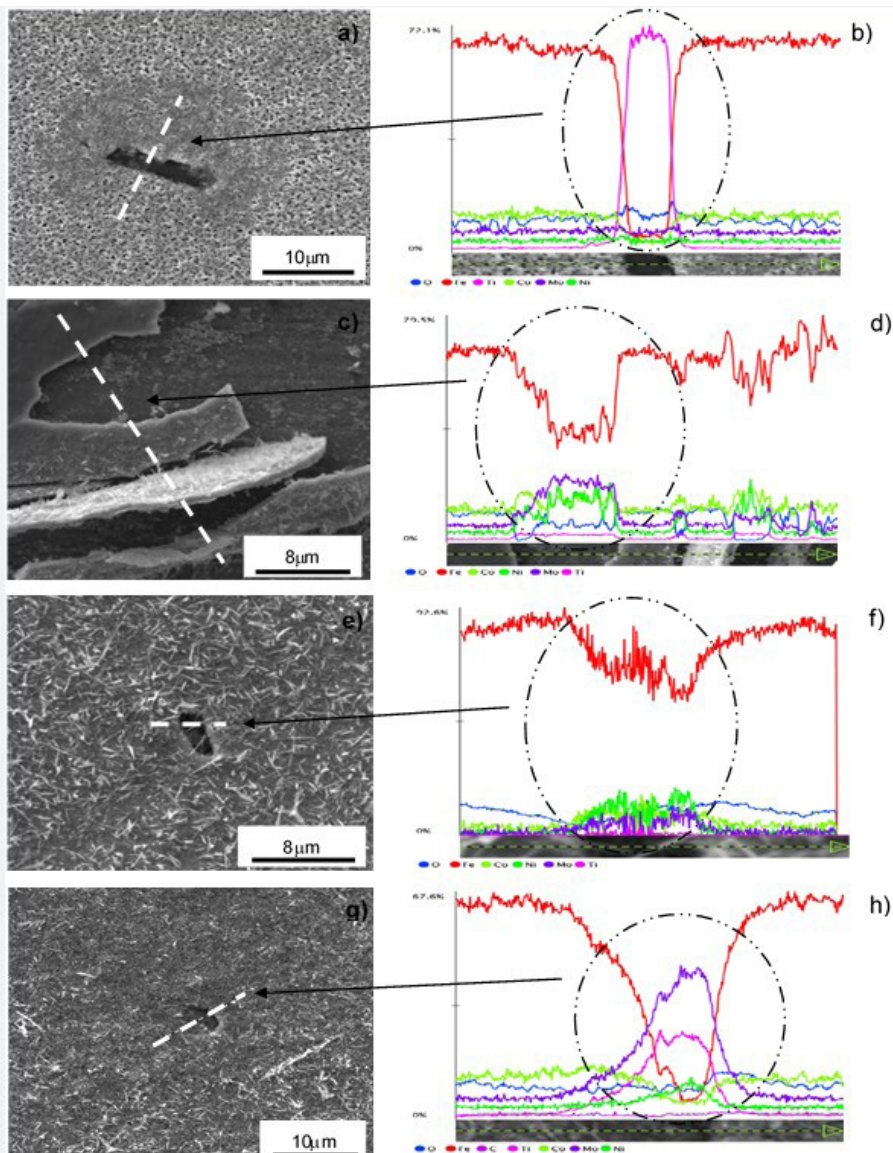


Figure 11. SEM and EDS spectrum of the oxide formed on grade 300 maraging steel in (a,b) O₂ atmosphere, (c,d) air atmosphere, and 350 maraging steel in (e,f) O₂ atmosphere and (g,h) air atmosphere.

used on the maraging alloys. To observe and determine the thickness of each oxide layer, cross-sections were done using the focused ion beam (FIB) technique. Figure 13 presents two field emission scanning electron microscopy (FE-SEM) micrographs performed on each oxide layer, one general and one magnified to observe the oxide in more detail and measure the thickness of the layer.

The oxides produced in the atmosphere with synthetic air in maraging steel 300 correspond to Figures 13a and 13b, and those formed in maraging steel 350 are in Figures 13c and 13d. On the other hand, the oxides produced in the atmosphere with O_2 in maraging 300 steel are in Figures 13e and 13f, and those formed in maraging 350 steel correspond to Figures 13g and 13h.

In all oxides, non-homogeneous thicknesses are observed and with several defects in the different layers of the films, such as porosity, small holes and roughness. Darker areas in the internal parts of the oxides are due to the junction of pores and the consequent formation of larger defects such as holes and even cracks, the generation of these phenomena is related to differences in the expansion coefficient between the different constitutive phases, as well as being related to chemical heterogeneities along with the oxide layer. In all the micrographs it is possible to observe the small fine-grained microstructure with a different shade just below the metal-oxide interface, it is an austenitic-rich phase in Ni and Co formed due to the oxidation process^{13-16,18}.

The oxides showed a dendritic-type metal-oxide interface, which was more evident in the micrographs of the oxides produced in maraging 300 steel. This phenomenon may be due to the oxidation process in which metal ions leave the

steel and travel through the oxide formed to the outermost layers^{13-15,18}. Table 8 shows the values of the average thickness measured for each oxide. The highest values were found in the oxide produced in maraging 300 steels (where the oxidation dendrites are more visible), which could indicate a greater susceptibility to oxidation of this steel, and this makes sense due to the greater amount of alloying elements that would bring some greater degree of stability to maraging steel 350^{1,7,18,29,30}.

The results on all oxides showed a heterogeneous layer, with different surface defects and formed by the same constitutive phases. The chemical composition of the oxide layer has variations from the metal/oxide interphase to the external surface. These differences are due the oxidation process of each element in the maraging alloy. Several authors commented about the formation and growth processes, and different points of view have been found. Klein et al.¹³, Florez et al.¹⁸, and Luo and Shen⁴⁸, mentioned that the formation of the oxide in maraging alloys at temperatures above 300 °C is explained by three different steps: (1) decomposition of the H_2O or O_2 , (2) dissociated oxygen are adsorbed on the steel surface and (3) oxidation

Table 8. Average thickness measured from the FE-SEM micrographs for the oxide produced by each condition.

Maraging alloy	Atmosphere	Thickness Average (μm)
300	Air	2.0
	O ₂	2.4
350	Air	1.6
	O ₂	1.3

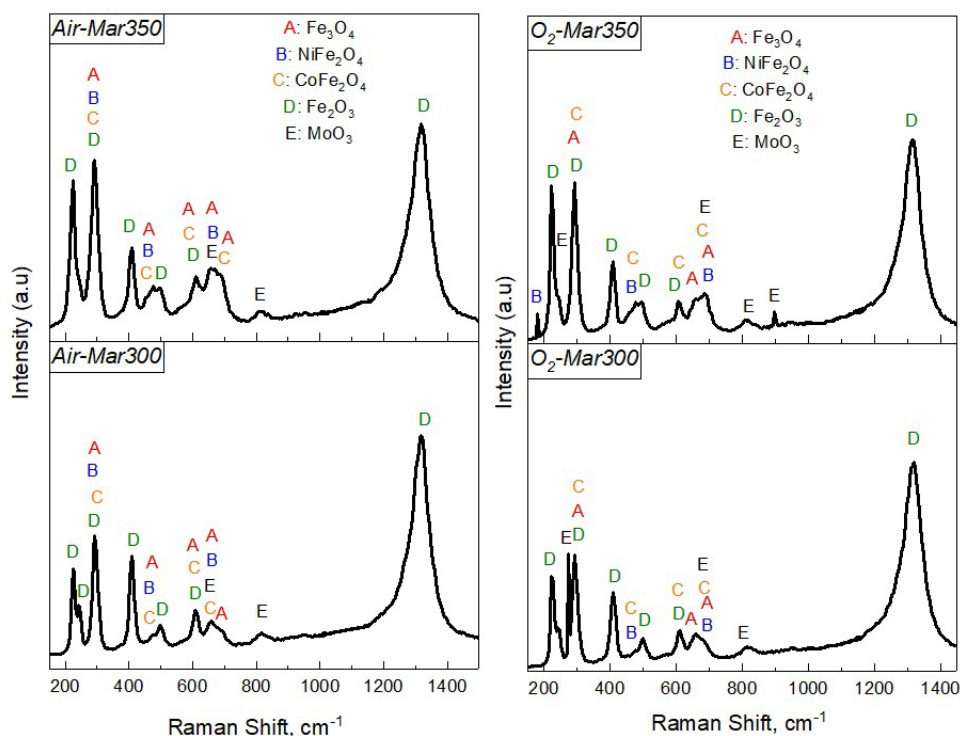


Figure 12. Raman spectra of the oxide layer growth under different atmospheres on maraging 300 and 350 alloy.

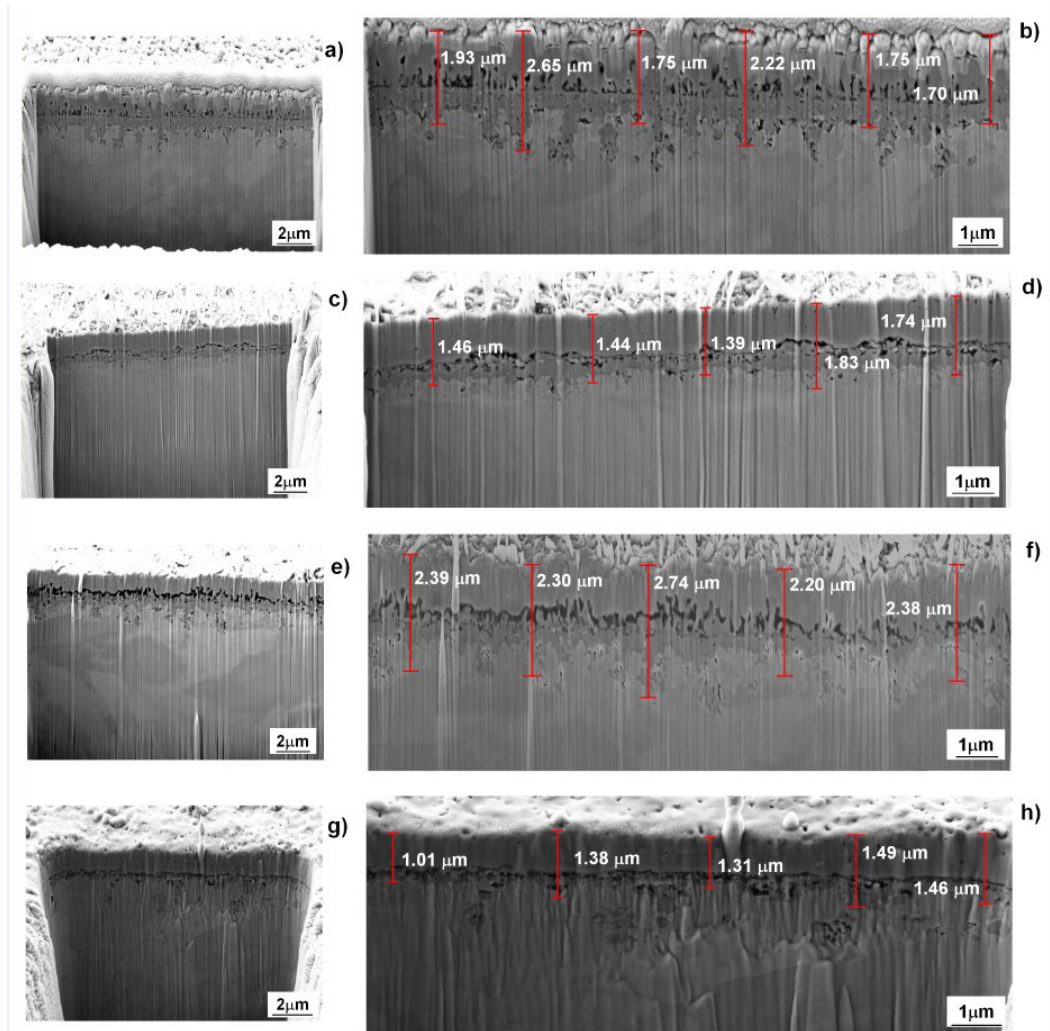
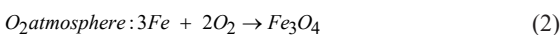
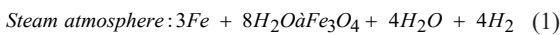


Figure 13. FE-SEM cross-section micrographs through the oxide layer produced using in air synthetic atmosphere on grade 300 (a,b) and 350 maraging steels (c,d) and O_2 atmosphere on grade 300 (e,f) and 350 maraging steels (g,h).

reactions between oxygen and metal ions. General oxidation reactions and thermodynamic parameters are presented by Klein et al.^{13,14} in order to explain the formation of an iron spinel, as shown in the following reactions:



Previous works mentioned the preferential formation of an iron ferrite (Fe_3O_4) during the maraging oxidation, and also commented that it is possible to find small quantities of Co and Ni as substitutional combinations in the magnetite microstructure, but not forming different compounds^{13-17,48-50}. However, in the present work, Ni and Co ferrites (NiFe_2O_4 and CoFe_2O_4) were found and fully identified within the oxide. The formation of these spinels are associated to the thermodynamic and kinetic conditions for the transformation of the previous magnetite formed by the diffusion of Co and Ni in the form of Co^{2+} and Ni^{2+} species from the metallic matrix. These

ions end up occupying the octahedral sites on magnetite, replacing the Fe^{2+} ion and displacing it to the outside of the film. In these new locations, the Fe^{2+} ions are exposed to a higher concentration of oxygen, then they are oxidized to Fe^{3+} as related in literature^{18,27,51-55}. These ions transform part of the magnetite in the other two spinels.

Due to the thermodynamic and kinetic conditions in temperatures ranged between 375 and 526 °C in oxygen rich atmospheres as used in the heat treatments, it is possible that the outermost layer of magnetite transforms into hematite ($\text{Fe}_3\text{O}_4 \rightarrow \alpha\text{-Fe}_2\text{O}_3$)^{18,49,50,56,57}. The transformation process occurs very fast depending on the chemical composition and the defects in the crystalline network^{18,55}. According to Genuzio et al.^{55,58} the hematite grows dendritically and has morphological differences comparing with the magnetite. These morphological differences are like the white elongated protuberances found in the oxides produced on both steels in all conditions.

Molibdenum was found in all oxide layer, with high quantities in the innermost part of the film. Mo formed

MoO₃ oxide as detected by XRD. It is important to mention that previous works commented that this type of compound was only in the inner parts of the oxide because Fe oxides have greater growth kinetics covering the other compounds, however, greater amounts of Mo and mainly Co in the composition steel chemistry allowed a greater availability of Mo for oxidation. Co decreases the solubility of Mo in steel which, during the thermal aging treatment, produces fine intermetallic precipitates rich in Mo^{1,7,18,29,30}.

TiO₂ is formed in the first stage of the oxidation process but due to its low kinetics, it is covered by the other compounds in the innermost parts of the oxide, and this is the reason why it was not detected by Raman spectroscopy^{18,49,59}.

Tribological properties in terms of scratch testing lead to determine the adhesive damage, known as the minimum interfacial

force between the oxide layer and the metallic substrate alloy and represent as *Pc*₂, as found in literature^{18,60,61}. Figure 14 (left-hand side) exhibits the whole scratch track made on the oxide produced on the steel and treatment described on each image.

The behavior is shown by comparing the micro-fracture events and damage features in regions close to track edges. Figure 14 (right-hand side) shows top-view FE-SEM images of nanoscratch tracks (corresponding to each oxide described on the side) where some interesting features and damage events are clearly visible (i.e. chevron cracks, decohesion, etc.). On the sides of all grooves, one can observe pile-ups as well as loose material in the form of flakes produced by the flow of plastically deformed material which is responsible for the serrated shape along the scratch track. Furthermore, the *Pc*₂ from the FESEM micrographs are summarized in Table 9.

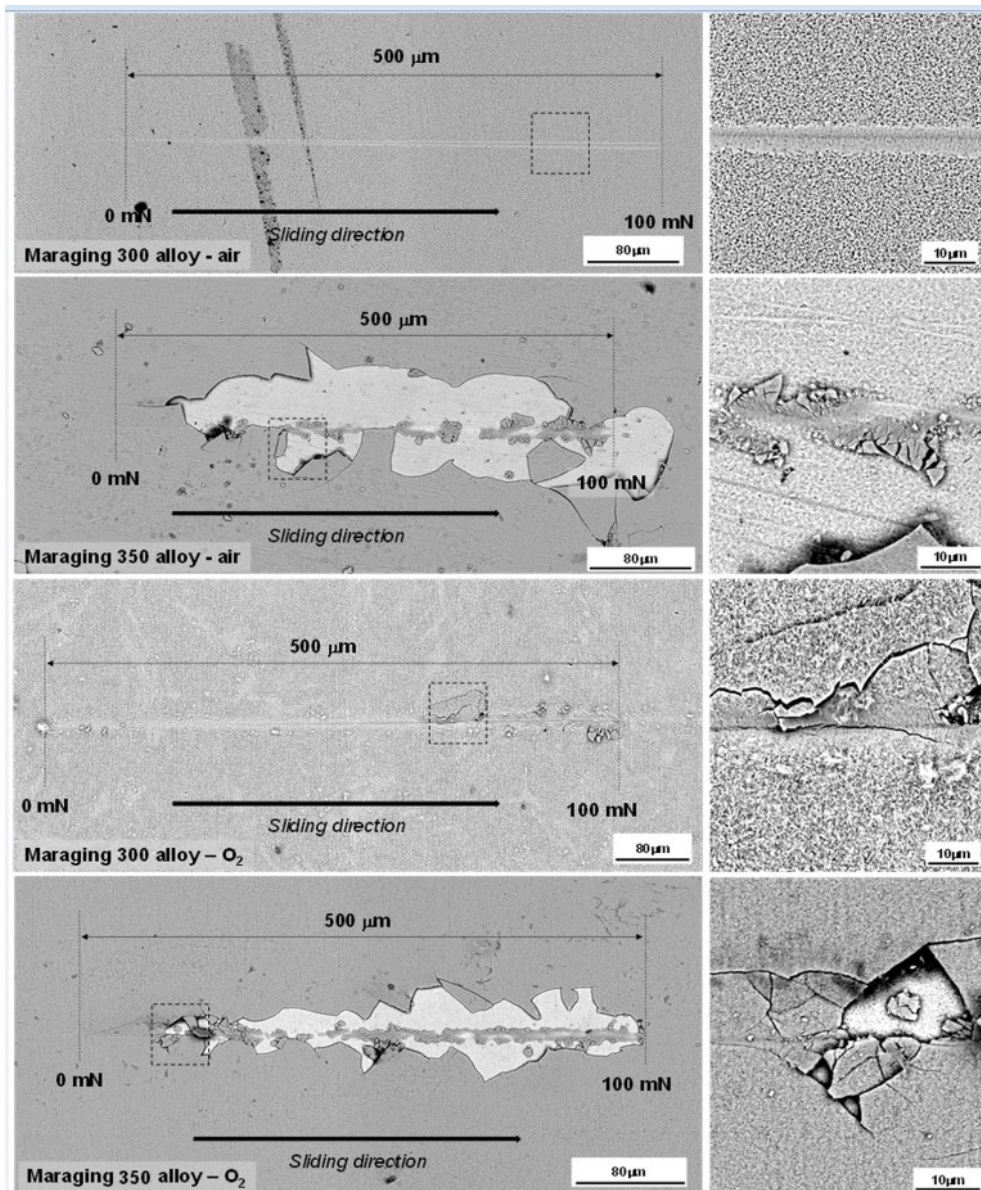


Figure 14. FE-SEM (left-hand side) image for the nanoscratch track and (right) magnification of the top-view FE-SEM images of nanoscratch tracks (made on each oxide produced on the steel and treatment described on left-side image) where the first adhesive damage appears.

Table 9. Pc2 directly determined from the FE-SEM micrographs for the oxide produced by each condition.

Maraging alloy	Atmosphere	Pc2 (mN)
300	Air	> 100
	O ₂	2
350	Air	65
	O ₂	5

From Figure 14 and the data summarized in Table 9, it can be shown that the oxide layers grown on maraging 300 alloy requires a higher force in order to produce the decohesion. On the other hand, the O₂ atmosphere produces an embrittlement of the oxide coating and a chipping effect is clearly visible while the oxide coating growth under air atmosphere does not present these damage mechanisms. Furthermore, as it is evident for maraging 300 alloy treated under air atmosphere, no decohesion is visible along the entire scratch track. A similar trend is observed for maraging 350 alloy. However, for this system, the adhesive load is 96% smaller than for the maraging 300 alloy. The oxide films produced in both maraging alloys using air atmosphere presents good adherence comparing with the result published by Florez et al.¹⁸ and Parizi et al.⁶¹, and the results of the oxides produced in air atmosphere show the capability for the use of tribological applications under sliding contact tests, and as coatings for improving the electrochemical behavior of maraging alloys and in equipments manufactured for use in processing minerals where it is subjected to wear^{18,61}.

4. Conclusions

The oxides produced in both maraging alloys presented heterogeneous oxide layer, with the presence of several defects spread on all the surface, such as holes, cracks and porosity. The differences in terms of roughness for all the samples do not indicate any relationship with the chemical composition for the different investigated alloys, therefore, it depends on the atmosphere used during the heat treatment itself.

It was possible to confirm the variable chemical composition from the innermost towards the oxide surface. Higher concentrations of alloy elements such Ni, Ti, Mo, and Co are found in the oxide layer/metal interface.

The phases present on the oxide layer grown in both conditions are iron spinel ferrite (Fe₃O₄), nickel spinel ferrite (NiFe₂O₄), cobalt spinel ferrite (CoFe₂O₄), hematite (Fe₂O₃), molybdenum oxide (MoO₃) and titanium oxide (TiO₂). It was found the lowest proportion of spinel on the oxides produced on maraging 350 alloy may be related to the chemical composition of the steel during the aging treatment, and a higher quantity of the intermetallic precipitates rich in Mo and Ti was produced.

The oxygen availability during the first stages of the heat treatment makes the kinetic and thermodynamic conditions suitable for the formation and growth of the hematite along with the oxide layer.

FIB cross-sections showed that the oxide films present a heterogeneous coating thickness. The oxides showed a dendritic-type metal-oxide interface, and this phenomenon probably may be related to the oxidation process. The highest thickness values were found in the oxide produced in maraging

300 steels which could indicate a greater susceptibility to oxidation of this steel.

The oxide film produced in both maraging alloys using air atmosphere presents excellent adherence between the oxide layer and the metallic substrate either under O₂ atmosphere. It demonstrates their capability for being used under aggressive conditions, such as coatings that can improve the electrochemical behavior of maraging alloys and in equipments manufactured for use in processing minerals where it is subjected to wear.

5. Acknowledgments

The authors gratefully acknowledge the CAPES/PRINT-UFSC and FUNCAP for financial assistance. The authors would like to thank the Central Analítica-UFSC (funded by Finep-CT-INFRA, CAPES-Pró-Equipamentos, and MCTI-CNPq-SisNano2.0) for the microscopy measurements, the Barcelona Research Center in Multiscale Science and Engineering – UPC, CIEFMA-UPC, LACAM-UFSC, and GPSA-UFSC Research Groups for technical support. Finally, J. J. Roa acknowledges the Serra Hunter programme of the “Generalitat de Catalunya”.

6. References

- Magnée A, Drapier JM, Dumont J, Coutsouradis D, Habraken L. Cobalt containing high strength steels [Internet]. Brussels: Centre d'Information du Cobalt; 1974. 128 p. [cited 2020 Mar 25]. Available from: [http://refhub.elsevier.com/S0360-3199\(19\)31930-5/sref1](http://refhub.elsevier.com/S0360-3199(19)31930-5/sref1)
- Silva MJG, Cardoso JL, Carvalho DS, Santos LP, Herculano LFG, Abreu HFG, et al. The effect of prior austenite grain size on hydrogen embrittlement of Co-containing 18Ni 300 maraging steel. *Int J Hydrogen Energy*. 2019;44(33):18606-15. <http://dx.doi.org/10.1016/j.ijhydene.2019.05.074>.
- Schmidt M, Rohrbach K. Heat treating of maraging steels. *ASM Int*. 1991;4:219-28. <http://dx.doi.org/10.31399/asm.hb.v04d.a0005948>.
- Rack HJ, Kalish D. The strength and fracture toughness of 18 Ni (350) maraging steel. *Metall Mater Trans, B, Process Metall Mater Proc Sci*. 1971;2(2):2011-3020. <http://dx.doi.org/10.1007/BF02814948>.
- Viswanathan UK, Dey GK, Asundi MK. Precipitation hardening in 350 grade maraging steel. *Metall Mater Trans, A Phys Metall Mater Sci*. 1993;24(11):2429-42. <http://dx.doi.org/10.1007/BF02646522>.
- Santos LPMD, Béréš M, Bastos IN, Tavares SSM, Abreu HFGD, Silva MG. Hydrogen embrittlement of ultra high strength 300 grade maraging steel. *Corros Sci*. 2015;101:12-8. <http://dx.doi.org/10.1016/j.corsci.2015.06.022>.
- Lima VX, Barros IF, Abreu HFGD. Influence of solution annealing on microstructure and mechanical properties of maraging 300 steel. *Mater Res*. 2016;20(1):10-4. <http://dx.doi.org/10.1590/1980-5373-mr-2016-0257>.
- Masoumi M, Abreu HF, Herculano LF, Pardal JM, Tavares SS, Silva MJ. EBSD study of early fractured phenomena in a 350 grade Maraging steel elbows exposed to hydrofluoric acid. *Eng Fail Anal*. 2019;104:379-87. <http://dx.doi.org/10.1016/j.engfailanal.2019.05.031>.
- Florez MAC, Pereira UC, Cardoso JL, Oliveira FJS, Araújo WS, Ribas GF, et al. Microstructural characterization of grade 300 and grade 350 maraging steels and electrochemical study in hydrofluoric solution. *J Fluor Chem*. 2021;243:109738. <http://dx.doi.org/10.1016/j.jfluchem.2021.109738>.

10. Glaser A. Characteristics of the gas centrifuge for uranium enrichment and their relevance for nuclear weapon proliferation. *Sci Glob Secur.* 2008;16(1-2):1-25. <http://dx.doi.org/10.1080/08929880802335998>.
11. Barzashka I, Oelrich I. Engineering considerations for gas centrifuges [Internet]. Washington: Federation of American Scientists; 2020 [cited 2020 Mar 25]. Available from: <https://fas.org/programs/ssp/nukes/fuelcycle/centrifuges/engineering.html#14>
12. Bradhurst DH, Heuer PM. Environmental Cracking of High Strength Maraging Steels: Part 2—Gaseous Fluoride Atmospheres. *Corrosion.* 1981;37(2):63-70. <http://dx.doi.org/10.5006/1.3593847>.
13. Klein IE, Sharon J, Yaniv AE. A mechanism of oxidation of ferrous alloys by super-heated steam. *Scr Metall.* 1981;15(2):141-4. [http://dx.doi.org/10.1016/0036-9748\(81\)90317-3](http://dx.doi.org/10.1016/0036-9748(81)90317-3).
14. Klein IE, Yaniv AE, Sharon J. The oxidation mechanism of Fe-Ni-Co alloys. *Oxid Met.* 1981;16(1):99-106. <http://dx.doi.org/10.1007/BF00603746>.
15. Klein IE, Yaniv AE, Sharon J. The mechanism of oxidation of Fe-Ni-Co alloys: the role of Ti and Mo. *Appl Surf Sci.* 1983;14(3-4):351-8. [http://dx.doi.org/10.1016/0378-5963\(83\)90048-X](http://dx.doi.org/10.1016/0378-5963(83)90048-X).
16. Rezek J, Klein IE, Yahalom J. Structure and corrosion resistance of oxides grown on maraging steel in steam at elevated temperatures. *Appl Surf Sci.* 1997;108(1):159-65. [http://dx.doi.org/10.1016/S0169-4332\(96\)00587-9](http://dx.doi.org/10.1016/S0169-4332(96)00587-9).
17. Greyling CJ, Kotzé IA, Viljoen PE. The kinetics of oxide film growth on Maraging steel as described by space-charge effects. *Surf Interface Anal.* 1990;16(1-12):293-8. <http://dx.doi.org/10.1002/sia.740160161>.
18. Florez MAC, Fargas Ribas G, Rovira JJR, Vilarrasa-Garcia E, Rodriguez-Castellon E, Sousa ABF, et al. Characterization study of an oxide film layer produced under CO₂/steam atmospheres on two different maraging steel grades. *Metals.* 2021;11(5):746. <http://dx.doi.org/10.3390/met11050746>.
19. Flamant Q, Garcia Marro F, Roa Rovira JJ, Anglada M. Hydrofluoric acid etching of dental zirconia. Part 1: etching mechanism and surface characterization. *J Eur Ceram Soc.* 2016;36(1):121-34. <http://dx.doi.org/10.1016/j.jeurceramsoc.2015.09.021>.
20. Dong WP, Sullivan PJ, Stout KJ. Comprehensive study of parameters for characterising three-dimensional surface topography: III: parameters for characterising amplitude and some functional properties. *Wear.* 1994;178(1-2):29-43. [http://dx.doi.org/10.1016/0043-1648\(94\)90127-9](http://dx.doi.org/10.1016/0043-1648(94)90127-9).
21. Dong WP, Sullivan PJ, Stout KJ. Comprehensive study of parameters for characterising three-dimensional surface topography: IV: parameters for characterising amplitude and some functional properties. *Wear.* 1994;178(1-2):45-60. [http://dx.doi.org/10.1016/0043-1648\(94\)90128-7](http://dx.doi.org/10.1016/0043-1648(94)90128-7).
22. Chung FH. Quantitative interpretation of X-ray diffraction patterns of mixtures. I. Matrix-flushing method for quantitative multicomponent analysis. *J Appl Cryst.* 1974;7(6):519-25. <http://dx.doi.org/10.1107/S0021889874010375>.
23. Zhou X, Liu D, Bu H, Deng L, Liu H, Yuan P, et al. XRD-based quantitative analysis of clay minerals using reference intensity ratios, mineral intensity factors, Rietveld, and full pattern summation methods: A critical review. *Solid Earth Sciences.* 2018;3(1):16-29. <http://dx.doi.org/10.1016/j.sesci.2017.12.002>.
24. Viana NF, Nunes CS, Abreu HFG. The variant selection in the transformation from austenite to martensite in samples of maraging-350 steel. *J Mater Res Technol.* 2013;2(4):298-302. <http://dx.doi.org/10.1016/j.jmrt.2013.03.017>.
25. Conde FF, Escobar JD, Oliveira JP, Béreš M, Jardini AL, Bose WW, et al. Effect of thermal cycling and aging stages on the microstructure and bending strength of a selective laser melted 300-grade maraging steel. *Mater Sci Eng A.* 2019;758:192-201. <http://dx.doi.org/10.1016/j.msea.2019.03.129>.
26. JCPDS International Center for Diffraction Data. Powder diffraction files. Swarthmore, PA, USA; 1975.
27. Dąbrowa J, Stygar M, Mięka A, Knapik A, Mroczka K, Tejchman W, et al. Synthesis and microstructure of the (Co, Cr, Fe, Mn, Ni) 3O₄ high entropy oxide characterized by spinel structure. *Mater Lett.* 2018;216:32-6. <http://dx.doi.org/10.1016/j.matlet.2017.12.148>.
28. Zhao N, Fan H, Zhang M, Ma J, Du Z, Yan B, et al. Simple electrodeposition of MoO₃ film on carbon cloth for high-performance aqueous symmetric supercapacitors. *Chem Eng J.* 2020;390:124477. <http://dx.doi.org/10.1016/j.cej.2020.124477>.
29. Vasudevan VK, Kim SJ, Wayman CM. Precipitation reactions and strengthening behavior in 18 Wt Pct nickel maraging steels. *Metall Trans, A, Phys Metall Mater Sci.* 1990;21(10):2655-68. <http://dx.doi.org/10.1007/BF02646061>.
30. Sha W, Cerezo A, Smith GDW. Phase chemistry and precipitation reactions in maraging steels: part IV. Discussion and conclusions. *Metall Mater Trans, A Phys Metall Mater Sci.* 1993;24(6):1251-6. <http://dx.doi.org/10.1007/BF02668193>.
31. Capurro C, Ciucci C. Analysis of titanium nitrides precipitated during medium carbon steels solidification. *J Mater Res Technol.* 2018;7(3):342-9. <http://dx.doi.org/10.1016/j.jmrt.2018.04.010>.
32. Silva CC, Farias JP, Miranda HC, Guimarães RF, Menezes JW, Marcelino MA No. Microstructural characterization of the HAZ in AISI 444 ferritic stainless steel welds. *Mater Charact.* 2008;59(5):528-33. <http://dx.doi.org/10.1016/j.matchar.2007.03.011>.
33. Petty ER. Martensite: fundamentals and technology. *J Appl Cryst.* 1970;4:402-3. <http://dx.doi.org/10.1107/S0021889871007349>.
34. Rodrigues AC, Bernardi HH, Otubo J. Microstructural analysis of Co-free maraging steel aged. *J Aerosp Technol Manag.* 2014;6(4):389-94. <http://dx.doi.org/10.5028/jatm.v6i4.400>.
35. Moshka O, Pinkas M, Brosh E, Ezersky V, Meshi L. Addressing the issue of precipitates in maraging steels—Unambiguous answer. *Mater Sci Eng A.* 2015;638:232-9. <http://dx.doi.org/10.1016/j.msea.2015.04.067>.
36. Kumar PR, Jung YH, Bharathi KK, Lim CH, Kim DK. High capacity and low cost spinel Fe₃O₄ for the Na-ion battery negative electrode materials. *Electrochim Acta.* 2014;146:503-10. <http://dx.doi.org/10.1016/j.electacta.2014.09.081>.
37. Robinson MR, Abdelmoula M, Mallet M, Coustel R. Starch functionalized magnetite nanoparticles: new insight into the structural and magnetic properties. *J Solid State Chem.* 2019;277:587-93. <http://dx.doi.org/10.1016/j.jssc.2019.06.033>.
38. Wang W, Ding Z, Zhao X, Wu S, Li F, Yue M, et al. Microstructure and magnetic properties of MFe₂O₄ (M = Co, Ni, and Mn) ferrite nanocrystals prepared using colloid mill and hydrothermal method. *J Appl Phys.* 2015;117(17):17A328. <http://dx.doi.org/10.1063/1.4917463>.
39. Gao X, Bi J, Wang W, Liu H, Chen Y, Hao X, et al. Morphology-controllable synthesis of NiFe₂O₄ growing on graphene nanosheets as advanced electrode material for high performance supercapacitors. *J Alloys Compd.* 2020;826:154088. <http://dx.doi.org/10.1016/j.jallcom.2020.154088>.
40. Routray KL, Saha S, Behera D. Nanosized CoFe₂O₄-graphene nanoplatelets with massive dielectric enhancement for high frequency device application. *Mater Sci Eng B.* 2020;257:114548. <http://dx.doi.org/10.1016/j.mseb.2020.114548>.
41. De la Figuera J, Quesada A, Martín-García L, Sanz M, Oujja M, Rebollar E, et al. Self-organized single crystal mixed magnetite/cobalt ferrite films grown by infrared pulsed-laser deposition. *Appl Surf Sci.* 2015;359:480-5. <http://dx.doi.org/10.1016/j.apsusc.2015.10.104>.
42. De Faria DLA, Lópes FN. Heated goethite and natural hematite: can Raman spectroscopy be used to differentiate them? *Vib Spectrosc.* 2007;45(2):117-21. <http://dx.doi.org/10.1016/j.vibspec.2007.07.003>.

43. Guo R, Dang L, Liu Z, Lei Z. Incorporation of electroactive NiCo₂S₄ and Fe₂O₃ into graphene aerogel for high-energy asymmetric supercapacitor. *Colloids Surf A Physicochem Eng Asp.* 2020;602:125110. <http://dx.doi.org/10.1016/j.colsurfa.2020.125110>.
44. Yang J, Xiao X, Chen P, Zhu K, Cheng K, Ye K, et al. Creating oxygen-vacancies in MoO_{3-x} nanobelts toward high volumetric energy-density asymmetric supercapacitors with long lifespan. *Nano Energy.* 2019;58:455-65. <http://dx.doi.org/10.1016/j.nanoen.2019.01.071>.
45. Reed BW, Williams DR, Moser BP, Koski KJ. Chemically tuning quantized acoustic phonons in 2D layered MoO₃ nanoribbons. *Nano Lett.* 2019;19(7):4406-12. <http://dx.doi.org/10.1021/acs.nanolett.9b01068>.
46. Almodóvar P, López ML, Ramírez-Castellanos J, Nappini S, Magnano E, González-Calbet JM, et al. Synthesis, characterization and electrochemical assessment of hexagonal molybdenum trioxide (h-MoO₃) micro-composites with graphite, graphene and graphene oxide for lithium ion batteries. *Electrochim Acta.* 2021;365:137355. <http://dx.doi.org/10.1016/j.electacta.2020.137355>.
47. Farzi-kahkesh S, Fattah A, Rahmani MB. Synthesis and optimum temperature determination of highly sensitive MoO₃-based heterojunction Schottky sensor for hydrogen detection. *Microelectron Eng.* 2021;235:111453. <http://dx.doi.org/10.1016/j.mee.2020.111453>.
48. Luo DW, Shen ZS. Oxidation behavior of Kovar alloy in controlled atmosphere. *Acta Metall Sin.* 2008;21(6):409-18. [http://dx.doi.org/10.1016/S1006-7191\(09\)60003-X](http://dx.doi.org/10.1016/S1006-7191(09)60003-X).
49. Subbaraman R, Deshmukh AS, Sankaranarayanan SK. Atomistic insights into early stage oxidation and nanoscale oxide growth on Fe (100), Fe (111) and Fe (110) surfaces. *J Phys Chem C.* 2013;117(10):5195-207. <http://dx.doi.org/10.1021/jp312514m>.
50. Jeon B, van Overmeere Q, Van Duin AC, Ramanathan S. Nanoscale oxidation and complex oxide growth on single crystal iron surfaces and external electric field effects. *Phys Chem Chem Phys.* 2013;15(6):1821-30. <http://dx.doi.org/10.1039/C2CP43490C>.
51. Tsukimura K, Sasaki S, Kimizuka N. Cation distributions in nickel ferrites. *Jpn J Appl Phys.* 1997;36(6R):3609-12. <http://dx.doi.org/10.1143/JJAP.36.3609>.
52. Rodrigues APG, Gomes DKS, Araújo JH, Melo DMA, Oliveira NAS, Braga RM. Nanoferrites of nickel doped with cobalt: influence of Co²⁺ on the structural and magnetic properties. *J Magn Magn Mater.* 2015;374:748-54. <http://dx.doi.org/10.1016/j.jmmm.2014.09.045>.
53. Bliem R, Pavelec J, Gamba O, McDermott E, Wang Z, Gerhold S, et al. Adsorption and incorporation of transition metals at the magnetite Fe₃O₄ (001) surface. *Phys Rev B Condens Matter Mater Phys.* 2015;92(7):075440. <http://dx.doi.org/10.1103/PhysRevB.92.075440>.
54. Pardavi-Horvath M. Microwave applications of soft ferrites. *J Magn Magn Mater.* 2000;215:171-83. [http://dx.doi.org/10.1016/S0304-8853\(00\)00106-2](http://dx.doi.org/10.1016/S0304-8853(00)00106-2).
55. Genuzio F, Sala A, Schmidt T, Menzel D, Freund HJ. Phase transformations in thin iron oxide films: spectromicroscopic study of velocity and shape of the reaction fronts. *Surf Sci.* 2016;648:177-87. <http://dx.doi.org/10.1016/j.susc.2015.11.016>.
56. Hong H, Memon NK, Dong Z, Kear BH, Tse SD. Flame synthesis of gamma-iron-oxide (γ-Fe₂O₃) nanocrystal films and carbon nanotubes on stainless-steel substrates. *Proc Combust Inst.* 2019;37(1):1249-56. <http://dx.doi.org/10.1016/j.proci.2018.06.098>.
57. Zhang X, Yang S, Yang Z, Xu X. Kinetics and intermediate phases in epitaxial growth of Fe₃O₄ films from deposition and thermal reduction. *J Appl Phys.* 2016;120(8):085313. <http://dx.doi.org/10.1063/1.4961607>.
58. Genuzio F, Sala A, Schmidt T, Menzel D, Freund HJ. Interconversion of α-Fe₂O₃ and Fe₃O₄ thin films: mechanisms, morphology, and evidence for unexpected substrate participation. *J Phys Chem C.* 2014;118(50):29068-76. <http://dx.doi.org/10.1021/jp504020a>.
59. Surman PL. The oxidation of iron at controlled oxygen partial pressures: I. Hydrogen/water vapour. *Corros Sci.* 1973;13(2):113-24. [http://dx.doi.org/10.1016/0010-938X\(73\)90023-1](http://dx.doi.org/10.1016/0010-938X(73)90023-1).
60. ASTM: American Society for Testing and Materials. ASTM/C1624: standard test method for adhesion strength and mechanical failure modes of ceramic coatings by quantitative single point scratch testing. West Conshohocken: ASTM; 2015.
61. Parizi MJG, Shahverdi H, Roa JJ, Pipelzadeh E, Martinez M, Cabot A, et al. Improving mechanical properties of glass fiber reinforced polymers through silica-based surface nanoengineering. *ACS Appl Polym Mater.* 2020;2(7):2667-75. <http://dx.doi.org/10.1021/acsapm.0c00295>.